A Molecular Logic Gate Enables Super-Resolved Imaging of Intracellular Lipid Droplets

Ádám Eördögh,[a,b] Carolina Paganini,[c] Dorothea Pinotsi,[d] Paolo Arosio,[c] and Pablo Rivera-Fuentes[a,b]*

[a]Laboratory of Organic Chemistry, ETH Zurich, 8093 Zurich, Switzerland
[b]Institute of Chemical Sciences and Engineering, EPF Lausanne, 1015 Lausanne, Switzerland
[c]Institute for Chemical and Bioengineering, ETH Zurich, 8093 Zurich, Switzerland
[d]Scientific Center for Optical and Electron Microscopy, ETH Zurich, 8093 Zurich, Switzerland

ABSTRACT: Photoactivatable dyes enable single-molecule imaging in biology. Despite progress in the development of new fluorophores and labeling strategies, many cellular compartments remain difficult to image beyond the limit of diffraction in living cells. For example, lipid droplets, which are organelles that contain mostly neutral lipids, have eluded single-molecule imaging. To visualize these challenging subcellular targets, it is necessary to develop new fluorescent molecular devices beyond simple on/off switches. Here, we report a fluorogenic molecular logic gate that can be used to image single molecules associated with lipid droplets with excellent specificity. This probe requires the subsequent action of light, a lipophilic environment and a competent nucleophile to produce a fluorescent product. The combination of these requirements results in a probe that can be used to image the boundary of lipid droplets in three dimensions with resolutions beyond the limit of diffraction. Moreover, this probe enables single-molecule tracking of lipids within and between droplets in living cells.

INTRODUCTION

Lipid droplets are cellular organelles present in nearly all cells, from bacteria to mammals. These cellular compartments consist of a core of neutral lipids and a phospholipid monolayer.[1,2] In addition to serving as storage sites of neutral lipids, these droplets participate in lipophagy,[3] various signaling processes,[4,5] and pathogen entry.[6] Prevalent human pathologies like diabetes, obesity and viral infections are thus related to lipid droplets.[7,8]

Light microscopy enables the direct observation of lipid droplets[9] and is therefore well suited to monitor the behavior of these organelles in live cells.[10] Fluorescent proteins, antibodies and hydrophobic small-molecule dyes have been reported as probes for lipid droplet imaging.[11] Among small-molecule probes, dye BODIPY 493/503,[12] aggregation-induced emission probes,[13,14] and merocyanine derivatives[15] have been employed. Although these probes are very useful in conventional microscopy applications, their resolution is limited by diffraction.[16–18] Single-molecule localization microscopy (SMLM) methods offer the highest spatial resolution among the super-resolved imaging tools that are applicable to living cells.[19] For widespread use of SMLM techniques, new probes with suitable optical properties are necessary to enable detailed imaging and visualization of lipid exchange and organelle interactions.

We envisioned that we could image lipid droplets at single-molecule resolution by employing a molecular logic gate with a strong fluorescent output. Recently, we showed that diazoindanone moieties spirofused to the core of xanthene dyes can be used to detect active enzymes in live cells with single-molecule resolution.[20,21] These probes take advantage of divergent pathways of the photoinduced Wolff rearrangement depending on the electronic properties

of the xanthene core. Upon irradiation, electron-rich xanthene scaffolds give fluorescent xanthene products, whereas electron-poor systems give ring-expanded dark products.[20,21] Diazoindanones spirofused to silicon-containing rhodamine dyes also undergo Wolff rearrangement to give two different products. It has been noted that the outcome of this photochemical reaction depends on the environment of the probe. For example, protein-bound conjugates rearrange preferentially into a fluorescent product, whereas molecules dissolved in aqueous solution give a ring-expanded, dark product (Scheme 1).[22]

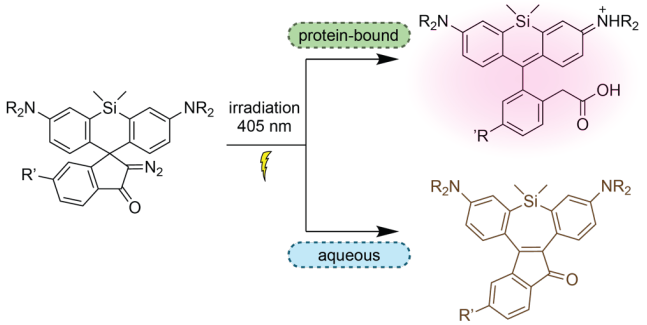

Scheme 1. Environment-sensitive photoactivation of silicon rhodamine diazoindanone

We hypothesized that we could use this environment sensitivity to create a probe that could give emit a fluorescent signal upon photoactivation in lipid droplets. Herein, we report the mechanism-based development of a probe for super-resolved imaging of lipid droplets and single-molecule tracking of lipid diffusion and exchange between these organelles.

RESULTS AND DISCUSSION

Mechanism of photoactivation. The photoinduced Wolff rearrangement of diazoindanones, such as compound **1**, can proceed following two general mechanisms depending on the substrate and reaction conditions (Figure 1):[23,24] a) Concerted loss of nitrogen and sigma-bond migration to form the ring-contracted ketene intermediate **2**, followed by trapping by a nucleophile to give fluorescent compound **3**, or b) loss of nitrogen leading to formation of carbene intermediate **4**, which would rearrange into the ring-expanded, dark product **5** (Figure 1). Based on these considerations and previous observations,[22] we hypothesized that formation of bright product **3** through the ketene intermediate is dominant in low polarity media. In contrast, carbene formation leading to **5** would be preferred in polar environments.

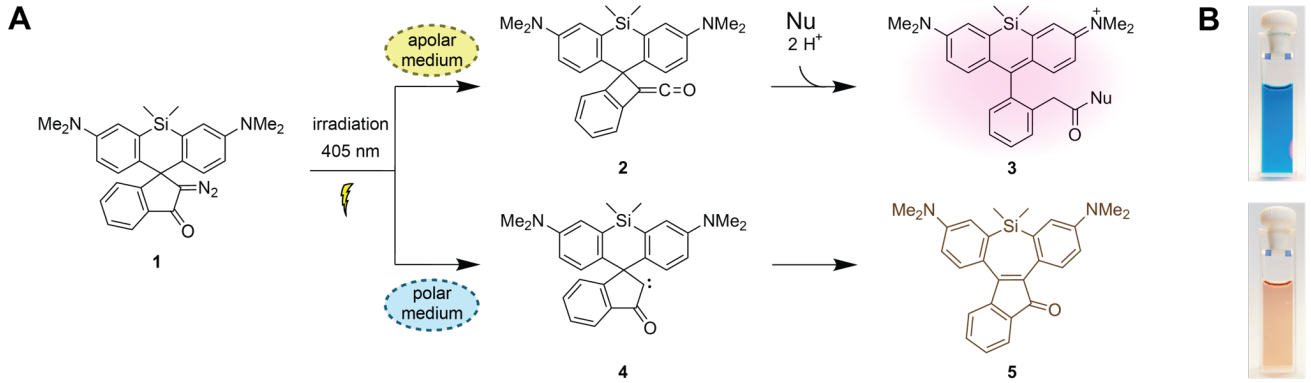

Figure 1. Photoactivation of probe **1**. A) Mechanism of the divergent pathways of the Wolff rearrangement depending on the polarity of the medium. B) Photographs of solutions of compounds **3** (blue solution) and **5** (pale brown) in MeOH.

To test this hypothesis, probe **1** was synthesized according to Scheme S1. Solutions of **1** (1 µm) in mixtures of primary alcohols and H_2O were irradiated. These solutions allowed for gradual control of polarity. The fluorescence of these solutions after photoactivation increased from pure H_2O to higher alcohol content (Figure 2A). When secondary or tertiary alcohols were used as media of photoactivation, lower fluorescence intensity was observed with decreasing nucleophilicity. Non-nucleophilic dioxane as solvent resulted in no fluorescence (Figure 2B). Addition of nucleophiles such as H_2O, MeOH and EtOH to irradiated solutions of **1** in dioxane (5 µm), led to an increase in fluorescence intensity (Figure 2C), which occurred immediately after addition of the nucleophile (Figure S1). Longer irradiation times resulted in formation of more fluorescent product (Figure 2C). These results are consistent with formation of the ketene intermediate **2** under low polarity conditions, followed by reaction with a nucleophile necessary to form fluorescent product **3** (Figure 1). Because several conditions must occur in order to form the fluorescent product, this system behaves as a multi-input AND logic gate (Figure 2D).
The proposed mechanism is further supported by irradiation experiments of **1** in dioxane-H_2O solvent mixtures. As expected, fluorescence increased from pure H_2O to dioxane H_2O 1:1 due to change in polarity. However, fluorescence decreased as less water was present to act as nucleophile, resulting in a maximum near 1:1 composition (Figure S1). Furthermore, irradiation of compound **1** in solvents mixtures with less nucleophilic organic component also led to lower conversion into fluorescent product, even when the polarity was kept constant (Figure S1).

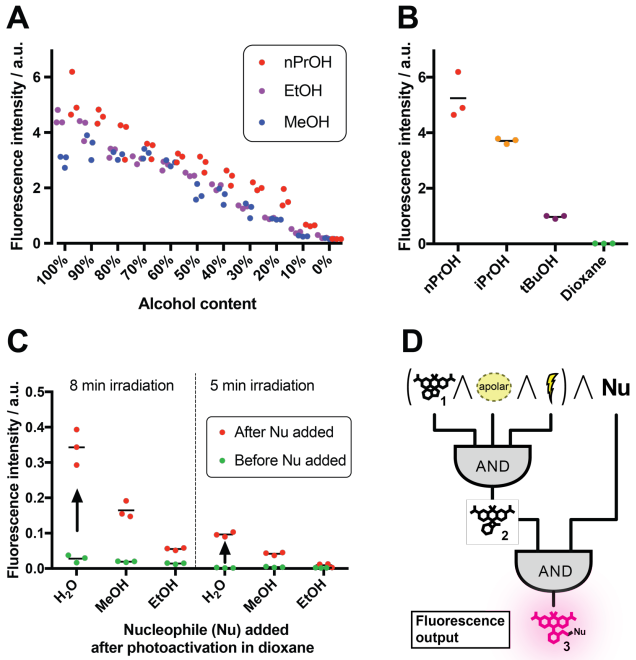

Figure 2. Formation of fluorescent product **3**. A) Fluorescence intensity upon irradiation of compound **1** (1 µm) in mixtures of primary alcohols and H_2O. B) Photoactivation of **1** (1 µm) in organic solvents with varying nucleophilicity. C) Initial readout was carried out on irradiated (5 or 8 min) solution of **1** (5 µM) in dioxane. 10% H_2O, MeOH, or EtOH were added as nucleophiles and second readout was performed. Photoactivation was carried out using a 405 nm transilluminator (2 mW cm^{-2}, 20 min). D) Photoreaction of **1** represented as a logic circuit with fluorescence output.

Analyses of irradiated samples in H_2O and different alcohols with liquid chromatography coupled to mass spectrometry (LC-MS) confirmed the identity of the proposed photoproducts **3** and **5**. Different alcohols yielded the corresponding esters of the fluorescent product in case of R = OMe, OEt, OPr

(Figure S2), confirming that the reaction proceeds through ketene **2**. This analysis also revealed that polarity not only changes selectivity of the reaction, but conversion of compound **1** was faster in apolar media (Figure S2). This observation is consistent with a higher quantum yield of photoconversion of compound **1** in MeOH compared to a mixture of MeCN-H_2O (Figure S3). The proposed intermediate of the alternative pathway, carbene **4**, was modeled in its singlet state by density functional theory (DFT) calculations at the B3LYP/def2-TVZPP level of theory. Carbene **4** was found as a minimum on the potential energy surface. Its large HOMO and LUMO coefficients on both the carbene and xanthene C-C bond in proximity suggest the possibility of rapid intramolecular insertion leading to **5** (Figure S4).

The structure of compound **1** and a derivative of compound **5** were further confirmed by X-ray crystallography (Figure S5). Additionally, the photophysical properties of compounds **1**, **3** and **5** were measured and compound **3** displayed high brightness (>27000 M^{-1} cm^{-1}) in both H_2O and organic solvents (Figure S6). We hypothesized that the low photochemical conversion or the change in selectivity in H_2O could be a consequence of aggregation of compound **1**. However, irradiation of compound **1** in an aqueous solution containing different amounts of sodium dodecyl sulfate (SDS) led to only a minor increase in formation of a fluorescent product (Figure S7). Furthermore, we synthesized compound **7** (Scheme S1), a derivative of compound **1** bearing a polyethylene glycol (PEG) chain, which had good solubility in H_2O. Irradiation of this compound in aqueous solution led to only minor formation of a fluorescent product, similarly to photoactivation of **1** (Figure S7). Furthermore, pH did not have an effect on the outcome of the photoreaction within a biologically relevant range (Figure S7).

These experiments suggest that the polarity of the medium is indeed responsible for the divergent reaction pathways. Based on this conclusion, we investigated the reason why polar media lead to carbene formation and apolar media to the ketene intermediate. First, we examined whether the polarity of the medium had an effect on the energy of the excited state. No solvatochromic shift in the absorption spectrum was observed, indicating that the HOMO-LUMO gap of **1** is not strongly sensitive to the environment of the molecule (Figure S8). Photoactivation with different wavelengths resulted in a slight change in the distribution of photoproducts, but the differences are modest compared to the effect of solvent polarity (Figure S8).

Having ruled out a significant contribution of solvatochromism, we investigated the involvement of triplet excited states. When solutions of compound **1** were irradiated in presence of the triplet sensitizer benzophenone, we observed a decrease in fluorescent product in all solvents (Figure S9). By populating the triplet excited state, we observed complete suppression of fluorescent product formation in apolar solvents; only non-fluorescent product **5** was formed (Figure S9). This result confirms that a triplet excited state favors formation of the carbene intermediate **4**. Because triplet sensitization completely suppressed formation of fluorescent product **3**, we can assume that ketene intermediate **2** does not form from carbene **4**. Instead, carbene **4** rearranges into dark product **5**. This reactivity is consistent with what has been found in diazo ketones adjacent to six-membered rings.[24]

Taking all these experiments into consideration, we propose that formation of product **3** or **5** is determined by whether intermediate **2** or **4** is generated. The selectivity between the two pathways is controlled by polarity, and a suitable nucleophile is essential for formation of fluorescent product **3**, making **1** a molecular logic gate with fluorescent output.

Labeling dynamics in synthetic lipid droplets. To evaluate the ability of compound **1** to label lipid droplets, we first tested this probe in model droplets generated in a microfluidic chip with a T-junction (Figure S10). To

mimic cellular lipid droplets, we produced emulsions of glyceryl trioctanoate in phosphate buffered saline (PBS) stabilized by SDS as surfactant. The size of resulting droplets was controlled by adjusting the flow rate of the two phases and ranged between 60–120 µm. Masked silicon rhodamine **1** was added to the oil phase, which was also labeled using BODIPY 493/503 as reference (Figure 3A-C).[12] Upon irradiation, the fluorescent signal developed in the aqueous phase close to the droplets and later dispersed within the channel. This observation suggests that the ketene precursor **2** is generated in the oil phase of the droplet, whereas fluorescent product **3** forms only upon contact of the ketene with nucleophilic H_2O molecules outside of the droplet (Figure 3D-E).

Next, we tested whether ketene **2** is formed in the oil phase of the droplet. To trap this intermediate within the droplet, we added the nucleophile 1-octanol (5%) to the oil phase and compound **1** was irradiated in this model system. In this case, the fluorescence develops first inside the droplet and at its periphery (Figure S11), whereas without octanol the droplets remained completely dark (Figure 3E). With 1-octanol as nucleophile in the oil phase, formation of the fluorescent octyl ester of compound **3** is expected. This C_8 carbon chain gives the molecule an amphipathic character, which localizes this bright product at the phase boundary of the biphasic system (Figure S11). Over time, however, this product also diffuses into the aqueous phase (Figure S11).

To enhance the interaction of the probe with the boundary of oil droplet, we synthesized probe **6**, a derivative of compound **1** functionalized with a palmitic acid substituent (Figure 3F and Scheme S1). The purpose of the saturated carbon chain was to anchor the polar fluorescent product to the oil droplet. Moreover, we envisioned that the negatively charged carboxylate functionality positions the dye near the phase boundary, well suited for the reaction with H_2O nucleophiles from the aqueous phase. Based on this reasoning, droplets were loaded with probe **6** and were irradiated. Fluorescence increased significantly at the boundary of the droplet, but not in its core or the outer aqueous phase (Figure 3G-J). This observation was further confirmed by three-dimensional imaging (z-stack acquisition) using a confocal microscope (Figure S12).

Compared to the unfunctionalized dye **1**, probe **6** persisted at the droplet boundary for longer time. By adding a palmitic acid moiety, we could turn the fluorescent logic gate **1** to probe **6**, that provides persistent signal at the boundary of model oil droplets. We anticipated that even in the complex environment of living cells, the combination of conditions needed to form fluorescent product of **6** would be fulfilled only at lipid droplets.

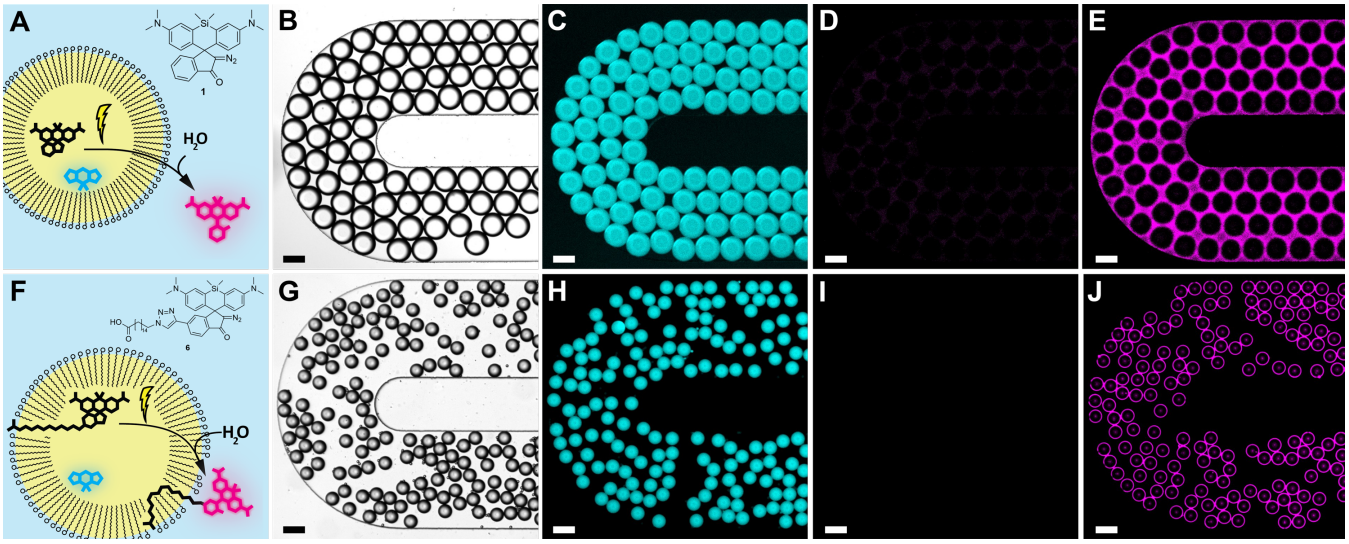

Figure 3. Photoactivation of compounds **1** and **6** in synthetic lipid droplets generated in a microfluidic system. A) Scheme of photoactivation and fluorescence generation of compound **1** in lipid droplets. The cyan structure represents BODIPY 493/503, the black structure represents compound **1** and fluorescent product **3** is shown in magenta. B) Bright field image of droplets containing BODIPY 493/503 and compound **1**. C) Fluorescence image of BODIPY 493/503. D) Fluorescence image of compound **1** before photoactivation. E) Fluorescence image of compound **1** after photoactivation. Fluorescence develops only outside of the droplet where H_2O can trap the formed ketene. F) Scheme of photoactivation and fluorescence generation of compound **6** in lipid droplets. The cyan compound represents BODIPY 493/503, the black structure represents compound **6** and its fluorescent product is marked with magenta. G) Bright field image of droplets containing BODIPY 493/503 and compound **6**. H) Fluorescence image of BODIPY 493/503. I) Fluorescence image of compound **6** before photoactivation. J) Fluorescence image of compound **6** after photoactivation. Fluorescence develops at the periphery of the droplet, where H_2O can trap the ketene and the palmitic acid substituents anchors the probe. Signal observed inside the droplet is out of-focus fluorescence from the periphery (Figure S12). Scale bars = 100 µm.

Live-cell imaging of intracellular lipid droplets. To test whether probe **6** labeled lipid droplets selectively in living cells, we induced formation of lipid droplets in HeLa cells using bovine serum albumin (BSA, 25 µM) complexed with oleic acid (200 µM). Cells were probe **6** (1 µM) for 18 h and BODIPY 493/503 (1 µM) as reference for 10 min. These cells were photoirradiated with a 405 nm laser to activate the probe. The signal that emerged from photoactivated compound **6** revealed a punctate pattern that co-localized with dye BODIPY 493/503 (Figure 4). Closer inspection of this signal revealed that, in fact, whereas BODIPY 493/503 stains the core of lipid droplets, fluorescence of photoactivated probe **6** gave ring-like structures that surround the core of the droplet (Figure 4C-D). This result confirms that probe **6** labels the periphery of lipid droplets selectively even in living cells.

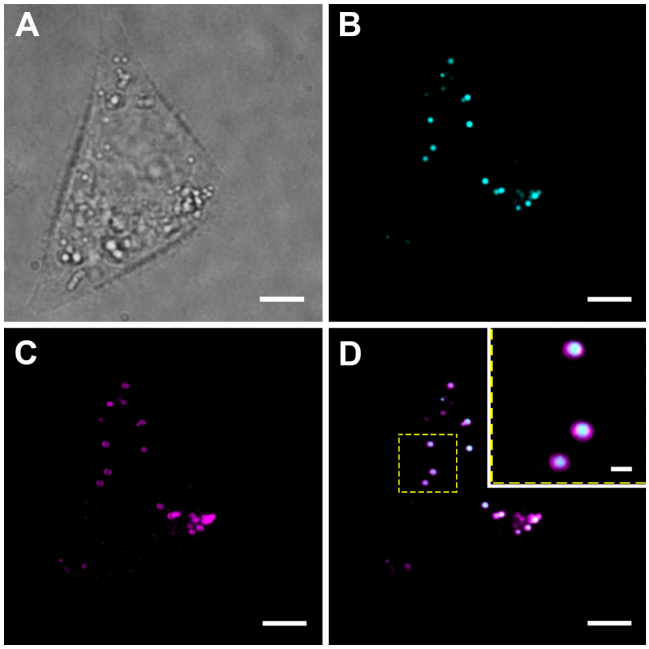

Figure 4. Confocal live-cell imaging of lipid droplets in HeLa cells using probe **6**. A) Bright field image of a HeLa cell loaded with BODIPY 493/503 and probe **6**. B) Fluorescent signal of lipid droplets stained with BODIPY 493/505. C) Fluorescent signal of compound **6** after photoactivation with 405 nm. D) Overlay of images (B) and (C) depicting the colocalization of probe **6** with lipid droplets. The inset displays the region enclosed by a yellow dotted rectangle. Scale bars: panel A–D = 3 µm, inset = 500 nm.

Unfunctionalized probe **1** also labeled the phase boundary of lipid droplets (Figure S13), albeit with lower specificity. Moreover, after photoactivation, probe **6** remains attached to the phospholipid monolayer of lipid droplets for significantly longer time than probe **1** (Figure S13), mirroring the results obtained using synthetic droplets. The greater specificity of probe **6** compared to compound **1** demonstrates that the palmitic acid substituent plays a role in keeping the probe aanchored to the phospholipid monolayer of the droplet. Finally, it was verified that probes **1** and **6** did not display cytotoxicity in HeLa cells. Methylthiazolyldiphenyl-tetrazolium bromide (MTT) cell viability assay confirmed that **1** is non-toxic within the concentration regime used for imaging. Although **6** displayed relatively high toxicity (IC_{50} = 4.68 µM), microscopy experiments could be carried out at lower concentrations (~1 µM) where high cell viability was observed (Figure S14).

SMLM of lipid droplets using probe 6. As a photoactivatable probe that labels the periphery of lipid droplets with high selectivity, compound **6** is ideally suited for SMLM. We performed 3D-SMLM in fixed cells with astigmatically distorted point-spread function (PSF) using adaptive optics in the light path.[25,26] The fixation procedure did not alter the labeling efficiency or specificity of probe **6**. Illumination of the fixed sample in highly inclined and laminated optical (HILO) mode with alternating events of photoactivation (405 nm, 0.1 ms pulse, 4 mW) and read-out (647 nm, 40 ms pulse, 125 mW, 25 pulses per 405 nm pulse) gave sparse activation of single molecules consistently through long acquisition sequences, well suited for live-cell SMLM. Observed lifetime values of single molecules (before photobleaching) were higher than other SMLM probes (τ = 5790 ± 750 s, mean ± 95% confidence interval -CI-, Figure S15).[27,28] The detected single molecules were fitted with an experimentally determined PSF approximated by cubic splines.[29] These signals

could be detected with an average localization precision of 32 ± 13 nm (mean ± standard deviation) in the lateral (x-y) plane, and 42 ± 17 nm (mean ± standard deviation) in the axial (z) direction, which is comparable to other 3D-SMLM studies (Figure S15).[30] The reconstructed, super-resolved images gave significant resolution enhancement over the diffraction-limited images taken simultaneously using either BODIPY 493/503 or compound **6** (Figure 5). For example, clusters of lipid droplets that could not be resolved by conventional microscopy are clearly visible in the reconstructed SMLM image (Figure 5C-E), and droplets that were out of focus could be resolved and localized precisely in space by 3D-SMLM with probe **6** (Figure 5E).

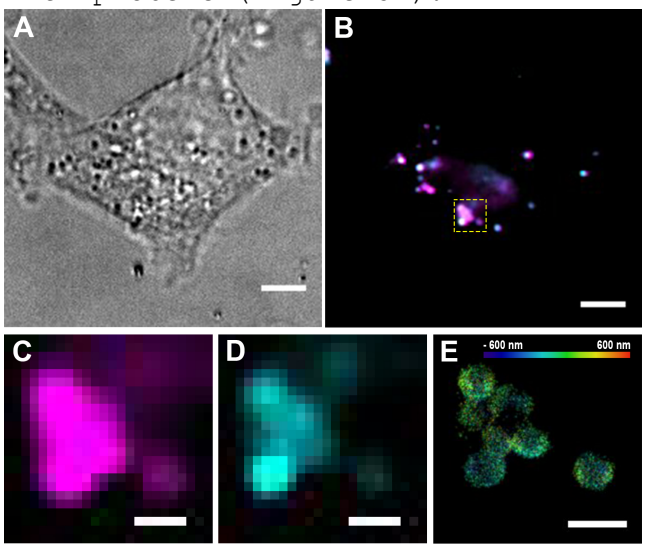

Figure 5. 3D-SMLM of lipid droplets in fixed HeLa cells. A) Bright field image of a HeLa cell. B) Overlay of diffraction limited (HILO illumination) images of droplets stained with BODIPY 493/503 and compound **6** after photoactivation. The region enclosed by a yellow dotted rectangle is displayed in panels C–E. C) Diffraction-limited image of lipid droplets using compound **6** after photo-activation. D) Diffraction-limited image of lipid droplets using BODIPY 493/503. E) Corresponding 3D-SMLM image obtained with compound **6**. The color bar indicates depth relative to an arbitrary focal plane. Scale bars: panels A-B = 5 µm; panels C–E = 1 µm.

HILO illumination is not a confocal technique. Therefore, the diffraction-limited images obtained with probe **6** (Figure 5 B-D) do not display the ring-like structures visible by spinning disk confocal microscopy (Figure 4). 3D-SMLM reconstruction, however, confirmed that probe **6** labels mainly the boundary of the droplets to give a shell-like volume with a dark core (Figure 6). From this volume, a discrete plane could be extracted and the resulting 2D plotting displays the ring-like structure, similar to what was observed with confocal microscopy (Figure 6 and Figure S16) This topology can be highlighted by plotting the localized single molecules colored by density (number of neighbors within 100 nm), which reveals that probe **6** gives low signal in the core of the droplet (Figure 6D).

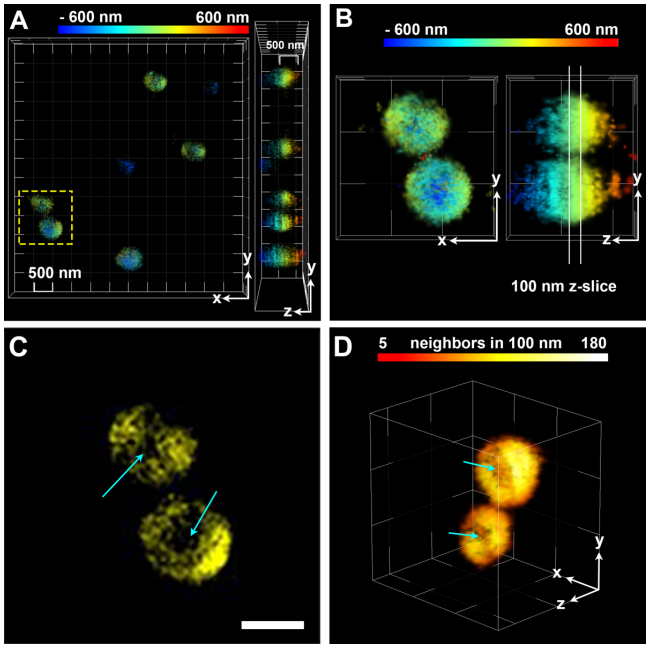

Figure 6. 3D structure of lipid droplets in fixed HeLa cells. A) 3D-SMLM of lipid droplets, color-coded by depth, viewed along the z and x axes. B) Selected lipid droplets for 2D rendering. C) 2D representation of the z-slice selected in panel B. This image corresponds to the x-y lateral plane. Cyan arrows indicate the absence of signals in the core of the droplet. D) 3D representation of single molecules on the phospholipid monolayer of lipid droplets. Signals are colored by density (number of neighbors withinin 100 nm). Cyan arrows indicate the less densely labeled core of the droplet. Scale bar: panel C = 500 nm. Tick marks in panels A, B and C = 500 nm.

Although the phospholipid monolayer of the droplet should be only a few nanometers wide, 3D-SMLM using compound **6** gives a shell that is 174 ± 28 nm (mean ± 95% CI) thick (Figure S16) according to data fitted with Gaussian curves (n = 8). One cause for the relatively low resolution are optical effects. Since the neutral lipids have a very different refractive index than the cytosol, the lipid droplet acts as a microscopic lens. Both in confocal and super-resolved images, we observed non-uniform intensity around the lipid droplet with two high intensity regions on opposite sides. We demonstrated that such intensity maxima rotate if the angle of HILO illumination is rotated around the z axis, confirming that the feature is an optical artefact (Figure S17). Therefore, it is important to take these optical effects into account when imaging lipid droplets with super-resolution.

Single-molecule tracking of fluorescent fatty acid probe 6. Besides providing enhanced resolution in lipid droplet imaging, probe **6** could also be used to track single-molecule dynamics of fatty acid molecules. For single-molecule tracking, we determined that the optimal illumination sequence consisted of alternated events of photoactivation (405 nm, pulsed 0.1 ms pulse, 4 mW) and read-out (645 nm, 40 ms pulse, 125 mW, 16 pulses per 405 nm pulse). These illumination conditions gave both the lowest lateral localization uncertainties and longest observed tracks (Figure S18). Average single-molecule track duration was estimated to be τ = 0.1461 ± 0.006 s (mean ± 95% CI), which is significantly longer than those of recently reported BODIPY dimers.[27] Moreover, with probe **6**, fluorescent molecules can be generated at any time point by an illumination pulse that provides a well-defined starting point for relatively long, uninterrupted tracks.

We performed initial tracking experiments in fixed cells to decouple the movement of single molecules from the movement of highly mobile lipid droplets. Counterstaining with BODIPY 493/503 was performed to assign the position of the droplet independently (Figure 7A-C). Under these conditions, single-molecule tracking revealed that about half of all tracks started within the lipid droplet (Figure S19). Single molecules outside of droplets traveled long distances with high diffusion coefficients ($D = 0.89 \pm 0.03\ \mu m^2\ s^{-1}$, mean ± 95% CI) and their tracks overlapped on specific regions (Figure 7D and inset). This observation suggests that these out-of-droplet molecules diffuse along other well-defined phospholipid layers in the cell, possibly the membrane of the endoplasmic reticulum.

Single-molecule tracks that started within a droplet also displayed high diffusion coefficients ($D = 0.79 \pm 0.03\ \mu m^2\ s^{-1}$, mean ± 95% CI), however, the majority of tracks (97%) terminated without the molecule leaving the droplet even after long acquisitions (Figure 7E). From the small fraction (3%) of molecules that left the droplet within an acquisition time of 200 s, most of them (~85%) left the droplet through specific regions (Figure 7F). Although a detailed characterization of these regions is beyond the scope of this study, we hypothesize that these may be contact points of lipid droplets with membranes of other organelles, for example the endoplasmic reticulum,[31] where lipid exchange can take place.

Finally, we demonstrated the applicability of **6** in live-cell single-molecule tracking. We recorded a 2D acquisition for single molecule tracking while also recording a diffraction limited reference frame every second to display positions of lipid droplets stained with BODIPY 493/503. Most particle tracks evolved within droplets reflecting the results obtained in fixed cells. The diffusion coefficients of fluorophores in live cells ($D = 0.87 \pm 0.03\ \mu m^2\ s^{-1}$, mean ± 95% CI) were only modestly different from those observed in fixed cells ($D = 0.85 \pm 0.03\ \mu m^2\ s^{-1}$, mean ± 95% CI). These observations suggest that the movement of the organelle does not affect significantly the measured diffusion coefficient of single molecules and fixation might not be necessary to obtain good quality single-molecule tracking data using probe **6**.

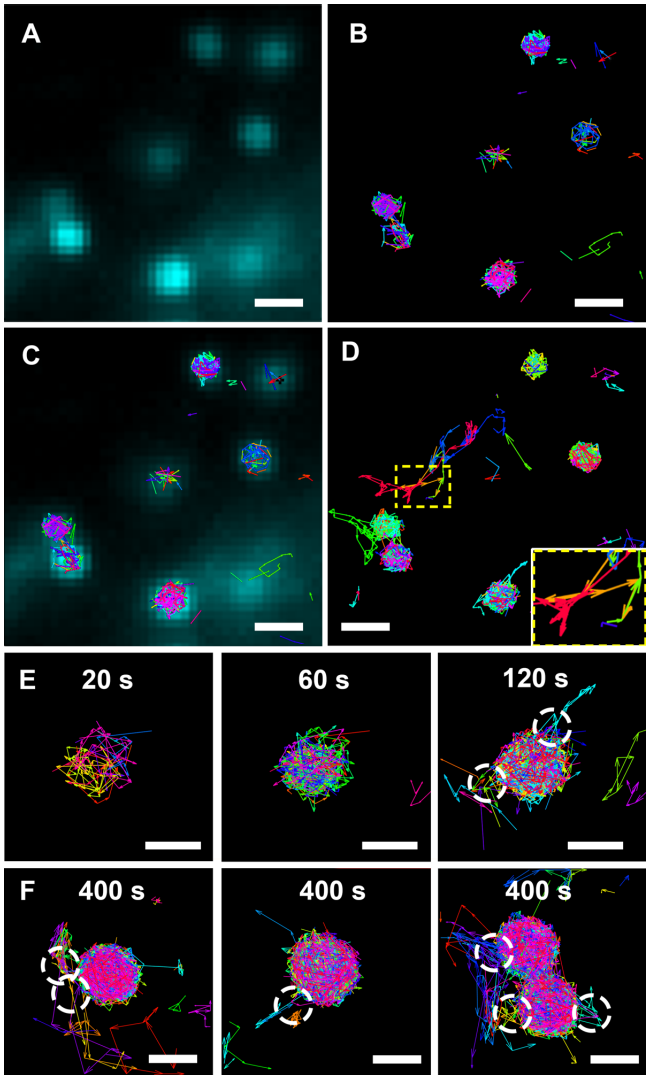

Figure 7. Single-molecule tracking in lipid droplets of HeLa cells. A) Lipid droplets of a fixed HeLa cell stained with BODIPY 493/503 as reference. B) Single molecule tracks observed during a 40 s acquisition. C) Overlay of (A) and (B). D) Single-molecule tracks from a 40 s acquisition (different time point than panel B), displaying molecules outside of droplets. E) Tracks evolving at a single droplet observed over 20, 60 and 120 s. Dotted white circles indicate regions where molecules leave the droplet. F) Tracks of molecules in different droplets acquired for 400 s. Dotted white circles indicate regions where molecules leave the droplet. Tracks of individual molecules are represented by a single color. Scale bars: panel A-D = 1 □m; panel E-F = 500 nm.

SUMMARY AND CONCLUSIONS

We explored the photochemistry of silicon-containing rhodamine diazoindanones, which release bright far-red fluorescent reporters upon irradiation with violet light. We confirmed that the photochemistry of these compounds is environment-dependent, with the fluorescent product favored in apolar environments. Fluorescent product formation takes place through a concerted Wolff rearrangement to yield a ketene, which subsequently reacts with a nucleophile. Both apolar environment and the presence of the nucleophile are essential to the formation of a bright fluorophore. We applied this molecular logic gate in oil droplet model systems and modified its structure to achieve sustained labeling of the periphery of lipid droplets. This anchoring mechanism was sufficient to target lipid droplets in live and fixed

cells. The excellent photophysical properties and targeting ability of the probe made it suitable for 3D-SMLM imaging in fixed cells as well as for 2D single-molecule tracking in ether fixed or live cells. Single-molecule imaging of this fatty acid probe was used to quantify molecular mobilities in lipid droplets, revealing specific sites of lipid exchange between droplets and their surroundings.

We envision that this concept of molecular logic gates for imaging could be extended to track single molecules in other apolar environments, such as membranes or membraneless organelles formed by liquid-liquid phase separation.

MATERIALS AND METHODS

General methods. Reagents were purchased from Alfa Aesar, Sigma Aldrich, ABCR, Fluorochem, Arcos, and TCI and were used as received. Solvents were procured from Fischer scientific and Acros and used as received. NMR spectra were acquired on Bruker 400-600 instruments. ^{1}H NMR chemical shifts are reported in ppm relative to $SiMe_4$ (δ = 0) and were referenced internally with respect to residual protons of the solvent. LC-MS chromatograms and mass spectra were acquired on Waters Aquity UPLC/MS spectrometer by using electrospray ionization (ESI). Data analysis and visualization was done in GraphPad Prism 7. High-resolution mass spectra (HRMS) were recorded by staff at the Molecular and Bioanalytical (MoBiAS) center of ETH Zurich. Stock solutions of **1**, **3**, **5**, **6**, and **S1** in DMSO were prepared at concentrations of 1 mM. X-ray structures were solved by staff at the Small Molecule Crystallography Center of ETH Zurich. Stock solutions were stored at −20 °C and were thawed immediately before experiments.

Optical Spectroscopy. UV-Visible spectra were obtained with a Cary 500 Scan spectrometer using quartz cuvettes of 10 mm pathlength (ThorLabs). Fluorescence spectra were acquired using a Fluorolog 3 fluorimeter (Horiba Jobin-Yvon). All measurements were carried out at room temperature and under red light ambient illumination. Extinction coefficients were determined by linear fit of five different concentrations of compound in PBS. Absolute fluorescence quantum yields were determined by means of an integrating sphere (Horiba Jobin-Yvon). Fluorescence intensity values after photoactivation were recorded with a Tecan Spark M10 plate reader. Excitation range was set to 625-645 nm detection in the 670-690 nm range. All spectroscopic measurements were carried out in triplicate.

Photoactivation of compounds 1 and 6. Photoactivation of compounds **1**, **6** and **7** was performed in an RPR-100 photoreactor (Rayonet), LCZ4 photoreactor (Luzchem) or an LED illuminator panel (in house). Illumination intensities follow as: LED transilluminator (λ_{max}= 405 nm, $P_{photonic}$ = 2 mW cm^{-2}, 50 min), 3 × RPR3500A Hg vapor light tubes (λ_{max} = 350 nm, $P_{photonic}$ = 0.85 mW cm^{-2}, 15 min), 3 × RPR3000A Hg vapor light tubes (λ_{max} = 300 nm, $P_{photonic}$ = 0.76 mW cm^{-2}, 50 min), for ketene solvolysis 16 × RPR3000A (λ_{max} = 300 nm, $P_{photonic}$ = ~7.1 mW cm^{-2}). For preparative reactions, quartz vessels were used for plate experiments non-covered Greiner Plate+ Glass coated 96-well plates with 150 µL liquid volume per well were used. For quantum yield of photoactivation of **1** (Figure S3), samples (150 µM, 3.0 mL) were prepared in MeOH and MeCN-H_2O (1:1) as solvents. Irradiation was performed in a quartz cuvette (Thorlabs) under constant magnetic stirring with an LED light source. Samples (35 µL) were taken during the irradiation (t = 0, 0.5, 1, 2, 3, 4, 6, 8, 10, 12, 15, 20, and 25 min) and subjected to HPLC analysis.

Photoactivation experiments in a microfluidic device. Microfluidic channels were fabricated by standard soft-lithography techniques. Polydimethylsiloxane (PDMS) was cased (Sylgard 184 kit; Dow Corning, Midland, MI, USA) on a master wafer (design shown in Figure S10), curing it at 65 °C for 75 min. The PDMS film was peeled off and bound to a glass slide after plasma activation to complete the device. The channel height was 60 µm. The channel width was

450 µm in the detection region and 50 µm at the nozzle. The flow in the channel was controlled by applying pressure at the inlets by using syringe pumps (Cetoni neMESYS, Cetoni GmbH, Korbussen, Germany). The applied flow rates were in the range of 0.1-0.5 µL min^{-1} for both phases. The oil phase consisted of glyceryl trioctanoate. When indicated, the oil phase was supplemented with 5% 1-octanol, 0.5 µM BODIPY 493/503 and 5 µM compound **1**. The aqueous phase was PBS (pH=7.4) with 1% w/w sodium dodecyl sulfate After filling the channels with lipid droplets, the flow was stopped and imaging began after 3 min waiting time to reduce the movement of droplets. Imaging of the microfluidic chips was carried out on a Nikon Eclipse T2 microscope equipped with an Andor Zyla 4.2 sCMOS camera. We used Nikon CFI Plan Fluor objectives 4x / 0.13, and 20x / 0.5 without optical fluid immersion. LEDMOD LAB Series – thermoelectric cooled high-power LED modules served as light sources controlled by Omikron Laserage light hub module. LED powers: 365 nm (250 mW), 445 nm (300 mW), and 671 nm (300 mW). Laser powers and exposure times were kept constant within a specific experiment. Measurements were conducted under low light ambient illumination to avoid photoactivation of the compounds.

Cell Culture. HeLa cells (ATCC CCL2) were grown in Dulbecco's Modified Eagle Medium (DMEM) supplemented with fetal bovine serum (FBS, 10%) and penicillin-streptomycin (0.1%) at 37 °C in a 95% humidity atmosphere under 5% CO_2 environment. Cells were grown to 90% confluence and seeded onto Ibidi chambered cover glass plates 48 h prior to imaging experiments. Before imaging, the growth medium was removed and the cells were washed with PBS (0.5 mL). Cells were subsequently incubated for the indicated time with 0.5 mL of imaging medium (Fluorobrite, Thermo Fisher Scientific) containing the fluorescent probe (10 µM) and imaged in the same medium.

Cell Viability Assay. The viability of HeLa cells was determined using methylthiazoluldiphenyl-tetrazolium bromide (MTT) assay. 9000 cells were seeded per well in 96-well plates and were grown to 90% confluency over a 24 h in growth medium. The cells were treated with compound **1** or **6** at different concentrations (0.2–100 µM). Dilution series of compound **1** and **6** were prepared in DMSO, of which volumes of 5 µL were added to growth medium (95 µL) to have the final concentration of DMSO constant. Positive controls were prepared with DMSO (0.5% v/v, 100% cell viability). After 48 h incubation with **1** or **6** the cells were treated with 10% MTT solution (5 g L^{-1}) in imaging medium (Fluorobrite) and incubated for 3 h. The supernatant was removed leaving the cells intact and 2-propanol (200 µL) was pipetted onto the wells. The plates were shaken in a microplate shaker for 10 min and the absorbance of individual wells was read out with a plate reader (SPARK 10M, TECAN). Six replicates were sampled at every concentration. IC_{50} values were determined with Prism 7 (GraphPad).

Lipid droplet induction. Lipid-droplet inducing medium was prepared by fatty acid-free bovine serum albumin (BSA, 25 µM) dissolved in growth medium consisting of Dulbecco's Modified Eagle Medium (DMEM), FBS (10%) and penicillin-streptomycin (0.1%). Oleic acid (200 µM) was added in ethanol stock solution (0.5 M). Probe **6** (1 µM) was added to the lipid droplet inducing medium. HeLa cells were plated onto Ibidi chambered cover glass plates. After the cells attached to the microscopy slide (24 h), the growth medium was changed to lipid droplet inducing medium for 24 h. This incubation resulted in reproducible lipid droplet formation in HeLa cells with droplet size around ~0.6 µm.

Confocal Imaging. Prior to imaging, the medium was removed, the cells were washed with PBS (pH = 7.4) and incubated with the defined concentration of probe **1** and **6** in phenol red-free imaging medium (FluoroBrite™ DMEM). After PBS wash cells were imaged in imaging medium. Confocal microscopy was performed with a Nikon Eclipse T1 microscope equipped with a Yokogawa spinning-disk confocal scanner unit CSU-W1-T2, a LUDL BioPrecision2 stage and an sCMOS camera (Orca Flash 4.0 V2). Nikon CFI Plan Apo TIRF objective was used 100x

/ 1.49 with oil immersion. Light sources were diode-pumped, solid-state lasers (DPSS) with the following illumination powers: 405 nm (10 mW), 488 nm (15 mW), and 647 nm (200 mW) measured at the tip of the optical fiber. The microscope was operated using Metamorph VisiVIEW software. Image analysis was performed using FIJI ImageJ 1.52g software.

SMLM Imaging. Lipid droplet formation was induced overnight in HeLa cells that were already attached to an Ibidi µ Slide 8-Well cover glass. Prior to imaging, the medium was removed, the cells were washed with PBS (pH = 7.4), and incubated with the BODIPY 493/503 reference dye. For cell fixation, cells were exposed to a solution of 4% paraformaldehyde (PFA) in PBS for 5 min. After subsequent PBS wash, the cells were imaged using a Nikon N-STORM microscope (Nikon, UK Ltd.) using an SR Apochromat TIRF 100x 1.49 N. A. oil immersion objective lens. Piezo-electronic focus-lock system (perfect focus system) was used to prevent axial drift during data acquisition. The illumination powers of light sources (solid-state lasers, Bruker) are reported as measured at the tip of the optical fiber. The emission was passed through filters with band pass windows at 502–538 nm and 660–780 nm. Fluorescence was detected with a Hamamatsu Orca Flash 4 v3 (6.5 × 6.5 µm pixel size) or a sCMOS camera with a 4x zoom lens in the light path. We confirmed that the observed signal is not from dimers of the BODIPY 493/503 reference dyes.[27] A MicAO 3dSR for SMLM (Imagine Optic, France) adaptive optics unit was inserted between the microscope side port and the camera, which was used to introduce aberration-free astigmatism for 3D SMLM. Ellipticity and orientation of ellipticity were used to acquire z coordinates of localizations.[25] A calibration z-stack with 10 nm steps was obtained using fluorescent 0.2 µm microspheres (TetraSpeck™, Invitrogen). Single-molecule signals were fitted with SMAP software[29] (3D, experimentally acquired PSF). Localizations with a localization precision above 80 nm (x-y) and 100 nm (z) were filtered out. Density filtering was used to remove intracellular background, keeping localizations with 1000 or more neighbors within a 800 nm radius. In a second step to filter background near droplets, localizations with 2 or more neighbors in a 45 nm radius were kept. Threshold values correspond to 22000 frame-long acquisition with 0.015 localizations μm^{-2} intracellular localization density. Super-resolved images were visualized with ThunderSTORM[32] and ViSP.[33]

Single-Molecule Tracking. For particle tracking, 2D acquisitions were carried out with the same Nikon N-STORM microscope, but using an Andor iXon DU888 camera (13 × 13 µm pixel size) and no adaptive optics unit for detection. Single-molecule signals were fitted with integrated Gaussians using the Thunderstorm[32] plugin of ImageJ. For Figure 7, projection of a 3D acquisition with ± 600 nm z-range was used. Synthetic image sequences were generated without excluding any localizations, which were analyzed with Diatrack 3.05.[34] Single-molecule tracks were generated if localizations were detected on three or more consecutive frames within a 0.8 µm radius. The radius was defined by the visually observed largest particle jump. The average intracellular labeling density in an experiment was 0.015 localizations μm^{-2} or lower. These settings resulted in a 1.5% probability of false linkage upon particle death in the most densely labeled field. Diffusion coefficients (D) were calculated using Diatrack for all individual tracks longer than 6 frames by fitting displacement squared values against time. More than 700 traces were averaged to obtain diffusion coefficient for one illumination sequence, and three fields of view were used to compare different conditions. Evolving particle tracks in live cells were visualized using the Mosaic[35] plugin for ImageJ.

Corresponding Author
*pablo.riverafuentes@epfl.ch

Notes

The authors declare no competing financial interest.

ACKNOWLEDGMENT

This work was supported by the Swiss National Science Foundation (grant 200021_165551 to P. R.-F.). All microscopy work was carried out at the Scientific Center for Optical and Electron Microscopy (ScopeM) at ETH Zurich. We thank Dr. Nils Trapp and Michael Solar (ETH Zurich) for X-ray structure determination. We thank Marie Kopp (ETH Zurich) for help with microfluidic experiments. We thank Dr. Pascal Valloton (ETH Zuich) for advice regarding particle tracking.

REFERENCES

(1) Olzmann, J. A.; Carvalho, P. Dynamics and Functions of Lipid Droplets. *Nat. Rev. Mol. Cell Biol.* **2018**, *20*, 137–155.

(2) Farese, R. V.; Walther, T. C. Lipid Droplets Finally Get a Little R-E-S-P-E-C-T. *Cell* **2009**, *139*, 855–860.

(3) Schulze, R. J.; Sathyanarayan, A.; Mashek, D. G. Breaking Fat: The Regulation and Mechanisms of Lipophagy. *Biochim. Biophys. Acta Mol. Cell Biol. Lipids* **2017**, *1862*, 1178–1187. https://doi.org/10.1016/j.bbalip.2017.06.008.

(4) Zechner, R.; Zimmermann, R.; Eichmann, T. O.; Kohlwein, S. D.; Haemmerle, G.; Lass, A.; Madeo, F. FAT SIGNALS - Lipases and Lipolysis in Lipid Metabolism and Signaling. *Cell Metab.* **2012**, *15*, 279–291.

(5) den Brok, M. H.; Raaijmakers, T. K.; Collado-Camps, E.; Adema, G. J. Lipid Droplets as Immune Modulators in Myeloid Cells. *Trends Immunol.* **2018**, *39*, 380–392.

(6) Vallochi, A. L.; Teixeira, L.; Oliveira, K. da S.; Maya-Monteiro, C. M.; Bozza, P. T. Lipid Droplet, a Key Player in Host-Parasite Interactions. *Front. Immunol.* **2018**, *9*, 1022.

(7) Krahmer, N.; Farese, R. V; Walther, T. C. Balancing the Fat: Lipid Droplets and Human Disease. *EMBO Mol. Med.* **2013**, *5*, 973–983.

(8) Greenberg, A. S.; Coleman, R. A.; Kraemer, F. B.; McManaman, J. L.; Obin, M. S.; Puri, V.; Yan, Q. W.; Miyoshi, H.; Mashek, D. G. The Role of Lipid Droplets in Metabolic Disease in Rodents and Humans. *J. Clin. Investig.* **2011**, *121*, 2102–2110.

(9) Digel, M.; Ehehalt, R.; Füllekrug, J. Lipid Droplets Lighting up: Insights from Live Microscopy. *FEBS Lett.* **2010**, *584*, 2168–2175.

(10) Ohsaki, Y.; Suzuki, M.; Fujimoto, T. Open Questions in Lipid Droplet Biology. *Chem. Biol.* **2014**, *21*, 86–96.

(11) Harris, L. A. L. S.; Skinner, J. R.; Wolins, N. E. Imaging of Neutral Lipids and Neutral Lipid Associated Proteins. *Methods Cell. Biol.* **2013**, *116*, 213–226.

(12) Listenberger, L. L.; Studer, A. M.; Brown, D. A.; Wolins, N. E. Fluorescent Detection of Lipid Droplets and Associated Proteins. *Curr. Protoc. Cell Biol.* **2016**, *35*, 24.2.1–24.2.11.

(13) Kang, M.; Gu, X.; Kwok, R. T. K.; Leung, C. W. T.; Lam, J. W. Y.; Li, F.; Tang, B. Z. A Near-Infrared AIEgen for Specific Imaging of Lipid Droplets. *Chem. Commun.* **2016**, *52*, 5957–5960.

(14) Wang, Z.; Gui, C.; Zhao, E.; Wang, J.; Li, X.; Qin, A.; Zhao, Z.; Yu, Z.; Tang, B. Z. Specific Fluorescence Probes for Lipid Droplets Based on Simple AIEgens. *ACS Appl. Mater. Interfaces* **2016**, *8*, 10193–10200.

(15) Collot, M.; Fam, T. K.; Ashokkumar, P.; Faklaris, O.; Galli, T.; Danglot, L.; Klymchenko, A. S. Ultrabright and Fluorogenic Probes for Multicolor Imaging and Tracking of Lipid Droplets in Cells and Tissues. *J. Am. Chem. Soc* **2018**, *140*, 5401–5411.

(16) Rust, M. J.; Bates, M.; Zhuang, X. Sub-Diffraction-Limit Imaging by Stochastic Optical Reconstruction Microscopy (STORM). *Nat. Methods* **2006**, *3*, 793–795.
(17) Betzig, E.; Patterson, G. H.; Sougrat, R.; Lindwasser, O. W.; Olenych, S.; Bonifacino, J. S.; Davidson, M. W.; Lippincott-Schwartz, J.; Hess, H. F. Imaging Intracellular Proteins at Nanometer Resolution. *Science* **2006**, *313*, 1642–1645.
(18) Sharonov, A.; Hochstrasser, R. M. Wide-Field Subdiffraction Imaging by Accumulated Binding of Diffusing Probes. *Proc. Natl. Acad. Sci. U. S. A.* **2006**, *103*, 18911–18916.
(19) Sauer, M.; Heilemann, M. Single-Molecule Localization Microscopy in Eukaryotes. *Chem. Rev.* **2017**, *117*, 7478–7509.
(20) Halabi, E. A.; Thiel, Z.; Trapp, N.; Pinotsi, D.; Rivera-Fuentes, P. A Photoactivatable Probe for Super-Resolution Imaging of Enzymatic Activity in Live Cells. *J. Am. Chem. Soc.* **2017**, *139*, 13200–13207.
(21) Thiel, Z.; Rivera-Fuentes, P. Single-Molecule Imaging of Active Mitochondrial Nitroreductases Using a Photo-Crosslinking Fluorescent Sensor. *Angew. Chem. Int. Ed.* **2019**, *58*, 11474–11478.
(22) Grimm, J. B.; English, B. P.; Choi, H.; Muthusamy, A. K.; Mehl, B. P.; Dong, P.; Brown, T. A.; Lippincott-Schwartz, J.; Liu, Z.; Lionnet, T.; Lavis, L. D. Bright Photoactivatable Fluorophores for Single-Molecule Imaging. *Nat. Methods* **2016**, *13*, 985–988.
(23) Kirmse, W. 100 Years of the Wolff Rearrangement. *Eur. J. Org. Chem.* **2002**, 2193–2256.
(24) Wang, Y.; Toscano, J. P. Time-Resolved IR Studies of 4-Diazo-3-Isochromanone: Direct Kinetic Evidence for a Non-Carbene Route to Ketene. *J. Am. Chem. Soc.* **2000**, *122*, 4512–4513.
(25) Huang, B.; Wang, W.; Bates, M.; Zhuang, X. Three-Dimensional Super-Resolution Imaging by Stochastic Optical Reconstruction Microscopy. *Science* **2009**, *319*, 810–813.
(26) Clouvel, G.; Jasaitis, A.; Sillibourne, J.; Izeddin, I.; Beheiry, M. El; Levecq, X.; Dahan, M.; Bornens, M.; Darzacq, X. Dual-Color 3D PALM/DSTORM Imaging of Centrosomal Proteins Using MicAO 3DSR. *Proc. SPIE*, **2013**, 85900Z.
(27) Smith, E. M.; Banerjee, C.; Puchner, E. M. Single-Molecule Localization Microscopy and Tracking with Red-Shifted States of Conventional BODIPY Conjugates in Living Cells. *Nat. Commun.* **2019**, *10*, 3400.
(28) Takakura, H.; Zhang, Y.; Erdmann, R. S.; Thompson, A. D.; Lin, Y.; McNellis, B.; Rivera-Molina, F.; Uno, S.; Kamiya, M.; Urano, Y.; Rothman, J. E.; Bewersdorf, J.; Schepartz, A.; Toomre, D. Long Time-Lapse Nanoscopy with Spontaneously Blinking Membrane Probes. *Nat. Biotechnol.* **2017**, *35*, 773–780.
(29) Li, Y.; Mund, M.; Hoess, P.; Deschamps, J.; Matti, U.; Nijmeijer, B.; Sabinina, V. J.; Ellenberg, J.; Schoen, I.; Ries, J. Real-Time 3D Single-Molecule Localization Using Experimental Point Spread Functions. *Nat. Methods* **2018**, *15*, 367–369.
(30) Jones, S. A.; Shim, S.-H.; He, J.; Zhuang, X. Fast, Three-Dimensional Super-Resolution Imaging of Live Cells. *Nat. Methods* **2011**, *8*, 499–505.
(31) Schuldiner, M.; Bohnert, M. A Different Kind of Love – Lipid Droplet Contact Sites. *Biochim. Biophys. Acta Mol. Cell Biol. Lipids* **2017**, *1862*, 1188–1196.
(32) Ovesný, M.; Křížek, P.; Borkovec, J.; Švindrych, Z.; Hagen, G. M. ThunderSTORM: A Comprehensive ImageJ Plug-in for PALM and STORM Data Analysis and Super-Resolution Imaging. *Bioinformatics* **2014**, *30*, 2389–2390.
(33) El Beheiry, M.; Dahan, M. ViSP: Representing Single-Particle Localizations in Three Dimensions. *Nat. Methods* **2013**, *8*, 689–690.
(34) Vallotton, P.; Olivier, S. Tri-Track: Free Software for Large-Scale Particle Tracking. *Microsc. Microanal.* **2013**, *19*, 451–460.

(35) Sbalzarini, I. F.; Koumoutsakos, P. Feature Point Tracking and Trajectory Analysis for Video Imaging in Cell Biology. *J. Struct. Biol.* **2005**, *151*, 182–195.